Original article

Pore-scale simulation of gas displacement after water flooding using three-phase lattice Boltzmann method

Sen Wang[1,2]*, Liyang Chen[1,2], Qihong Feng[1,2], Li Chen[3], Chao Fang[4], Ronghao Cui[5]

[1]*Key Laboratory of Unconventional Oil & Gas Development, Ministry of Education, Qingdao 266580, P. R. China*

[2]*School of Petroleum Engineering, China University of Petroleum (East China), Qingdao 266580, P. R. China*

[3]*Key Laboratory of Thermo-Fluid Science and Engineering of MOE, School of Energy and Power Engineering, Xi'an Jiaotong University, Xi'an 710049, P. R. China*

[4]*Department of Chemical and Biomolecular Engineering, University of California Berkeley, Berkeley, California 94720, USA*

[5]*Physical Science and Engineering Division, Computational Transport Phenomena Laboratory, King Abdullah University of Science and Technology, Thuwal 23955-6900, Saudi Arabia*

Abstract:
Water flooding is a commonly used technique to improve oil recovery, although the amount of oil left in reservoirs after the procedure is still significant. Gas displacement after water flooding is an effective way to recover residual oil, but the occurrence state and flow principles of multiphase fluid after gas injection are still ambiguous. Therefore, the gas displacement process after water flooding should be studied on the pore scale to provide a basis for formulating a reasonable gas injection program. Most of the current pore-scale studies focus on two-phase flow, while simulations that account for the influence of oil-gas miscibility and injected water are seldom reported. In this work, the multi-component multi-phase Shan-Chen lattice Boltzmann model is used to simulate the gas displacement after water flooding in a porous medium, and the effects of injected water, viscosity ratio, pore structure, and miscibility are analyzed. It is established that the injected water will cause gas flow path variations and lead to premature gas channeling. Under the impact of capillary pressure, the water retained in the porous medium during the water flooding stage further imbibes into the tiny pores during gas injection and displaces the remaining oil. When miscibility is considered, the oil-gas interface disappears, eliminating the influence of the capillary effect on the fluid flow and enabling the recovery of remaining oil at the corner. This study sheds light on the gas displacement mechanisms after water flooding from the pore-scale perspective and provides a potential avenue for improving oil recovery.

1. Introduction

The water flooding technology has been widely used to improve oil recovery rates; however, most oilfields have entered the high water cut stage. Continuous water flooding has little effect on improving oil recovery (Ji et al., 2012). Gas displacement can further enhance the recovery factor of high water-cut reservoirs and lead to long-term stable production in oilfields (Preston et al., 2005; Kong et al., 2021). In addition to raising the recovery factor, gas injection has additional advantages. For example, CO_2 injection can contribute to reducing carbon emissions by geological storage, mitigating the problems of global warming and environmental pollution (Ren et al., 2016, 2022; Liu et al., 2022b), and hydrocarbon gas injection can help to regulate natural gas peaks in different seasons (Davarpanah et al., 2019; Mazarei et al., 2019; Cao et al., 2020; Liu et al., 2022c). However, due to the influence

of various factors such as reservoir heterogeneity and the oil-gas-water viscosity difference, the injected gas may transport quickly and reach the bottom hole of the production well much earlier, impeding the oil production rate and causing ineffective gas circulation in the rock stratum. This reduces the recovery factor of oil reservoirs and their gas storage capacity, which is unfavorable for gas injection (Qu et al., 2020; Zhao et al., 2020; Shen et al., 2021). Therefore, it is necessary to understand the gas flow mechanisms in a porous medium after water injection, in order to lay a solid basis for effective gas injection program design and enhanced oil recovery.

Several experimental studies have attempted to understand gas flooding behaviors. Hustand and Torleif (1992) analyzed gravity-stabilized hydrocarbon gas displacement after water flooding using core-scale experiments. They injected gas from the top and bottom of the core separately, and reported that oil banks formed in both cases. They further analyzed the effects of oil-gas relative permeability, capillary force, and composition variations on the oil recovery. Sohrabi et al. (2008a, 2008b) explored the mechanisms of near-miscible gas flooding and water alternating gas flooding using a high-pressure glass micromodel, and suggested that near-miscible gas flooding enhances flow and cross-flow between the bypassed pores and the injected gas, which significantly contributes to oil recovery. Alemu et al. (2013) carried out CO_2 displacement experiments with core samples adopted from the parallel and perpendicular directions of the formation. Three-dimensional images of fluid distribution and saturation during the displacement were obtained using an industrial X-ray CT scanner, and the results showed that the layering and displacement direction have significant effects on the fluid distribution. The experiments of Tovar et al. (2014) revealed that CO_2 permeated through the shale matrix from the fractures and almost all of the oil was recovered.

Despite the above advances, core-scale experiments, especially those requiring the generation of high pressure and temperature, are costly and time-consuming. It is difficult to reveal the gas transport mechanisms in the cores, as the images of continuous dynamics cannot be obtained experimentally with high temporal and spatial precision (Andrew et al., 2014). Pore-scale simulations can complement experimental studies and have become an efficient and economical approach in exploring flow behaviors (Feng et al., 2020; Zhu et al., 2022). In the past ten years, the lattice Boltzmann method (LBM) based on dynamic theory has evolved into a powerful computational fluid dynamics tool because of its advantages in the easy implementation of complex boundaries, auto-tracking phase interface, and natural parallelism (Zhang, 2011; Li et al., 2013; Zeidan et al., 2019). LBM has been widespread in the simulations of multiphase flow in the porous medium, chemical reactions, and heat transfer process (Chen et al., 2013, 2015; Golparvar et al., 2018; Zhang et al., 2021; Wei et al., 2022). At present, the commonly utilized multiphase models include the Shan-Chen model, the color gradient model (Diao et al., 2021; Liu et al., 2022a), and the phase field model (Wang et al., 2019). These have been described in detail by Liu et al. (2016). Some models have been extended to three-phase systems. Zhang et al. (2019) employed a multi-relaxation time

lattice Boltzmann model to study the relative permeability of three immiscible fluids in a 3D random porous medium and analyzed the effects of capillary number, wettability, and viscosity ratio. Tang et al. (2019) used the three-phase LBM model to analyze the flow behavior of water, oil, and CO_2 in a porous medium, and explored the microscopic displacement of CO_2 in rocks under different injection conditions. Wei et al. (2020) studied the process of slug-assisted water injection at the pore scale using the three-phase Shan-Chen model and summarized the enhanced oil recovery mechanisms in different porous structures. Li et al. (2021) investigated the displacement process in a simple pore-throat connection model, and suggested that an oil layer spreading over the gas-water interface would form under supercritical conditions, leading to a higher oil recovery regardless of the wetting properties of the solid surface. On the basis of the pore-scale three-phase flow simulation results, Zhu et al. (2022) identified some typical microscopic displacement behaviors, including coalescence and split-up, pinch-off, double and multiple displacement, as well as parallel flow. However, there are few reports on the three-phase flow mechanisms of gas displacement after water flooding (GDAWF).

In this work, the multi-component multi-phase (MCMP) Shan-Chen model is utilized to study three-phase flow behavior in a porous medium during gas displacement after water flooding while considering the effects of different factors, such as injected water, viscosity ratio, pore structure, and oil-gas miscibility.

2. Numerical method

In the MCMP model, each fluid component (i.e., oil, water, or gas phase) requires a distribution function. The lattice Boltzmann equation with external force term is given by (Zhao et al., 2017):

$$f^{\sigma}(\boldsymbol{x} + c\boldsymbol{e}\delta_t, t + \delta_t) - f^{\sigma}(\boldsymbol{x},t) = -(M^{-1}S^{\sigma}M)(f^{\sigma}(\boldsymbol{x},t) - f^{\sigma(eq)}(\boldsymbol{x},t)) + \left[M^{-1}(I - \frac{S^{\sigma}}{2})M\right]\overline{F}^{\sigma}(x,t) \quad (1)$$

where $f^{\sigma}(\boldsymbol{x},t)$ stands for the density distribution function of component σ at position $\boldsymbol{x}$ and time t; $c = \delta_x/\delta_t$ represents the lattice velocity, and δ_x and δ_t are the lengths of each lattice and time step, respectively (i.e., 1); I is the unit diagonal matrix of order nine. The collision operator adopts the multi-relaxation time format to improve the simulation stability and accuracy. The parameter $\boldsymbol{e}$ is the discrete velocity direction, and the values of different directions in the D2Q9 model are as follows:

$$\boldsymbol{e} = \begin{pmatrix} 0 & 1 & 0 & -1 & 0 & 1 & -1 & -1 & 1 \\ 0 & 0 & 1 & 0 & -1 & 1 & 1 & -1 & -1 \end{pmatrix} \quad (2)$$

Furthermore, $f^{\sigma(eq)}(\boldsymbol{x},t)$ is the equilibrium distribution function of component σ, expressed as:

$$f_i^{\sigma(eq)}(\boldsymbol{x},t) = \rho_\sigma \omega_i \left[1 + \frac{3}{c^2} \left(\boldsymbol{e}_i \cdot \boldsymbol{u}_\sigma^{eq} \right) \right.$$
$$\left. + \frac{9}{2c^4} (\boldsymbol{e}_i \cdot \boldsymbol{u}_\sigma^{eq})^2 - \frac{3}{2c^2} |\boldsymbol{u}_\sigma^{eq}|^2 \right] \quad (3)$$

where ω_i denotes the weight of each direction, $\omega_0 = 4/9$, $\omega_{1-4} = 1/9$, and $\omega_{5-8} = 1/36$. In the MCMP model, the equilibrium velocity $\boldsymbol{u}_\sigma^{eq}$ is defined as:

$$\boldsymbol{u}^{eq} = \frac{\sum_\sigma s_\rho^\sigma \rho_\sigma \boldsymbol{u}_\sigma}{\sum_\sigma s_\rho^\sigma \rho_\sigma} \quad (4)$$

where ρ_σ and $\boldsymbol{u}_\sigma$ represent the density and velocity of component σ, respectively, and are estimated by:

$$\rho_\sigma = \sum_i f_i^\sigma, \rho_\sigma \boldsymbol{u}_\sigma = \sum_i \boldsymbol{e}_i f_i^\sigma + \frac{\delta^t}{2} \boldsymbol{F}^\sigma \quad (5)$$

The transform matrix M in Eq. (1) is used to transform the distribution function f^σ and equilibrium distribution function $f^{\sigma(eq)}$ from velocity space to momentum space, which can be constructed from the discrete velocities via the Gram-Schmidt orthogonalization procedure (Yu et al., 2019):

$$M = \begin{bmatrix} 1 & 1 & 1 & 1 & 1 & 1 & 1 & 1 & 1 \\ -4 & -1 & -1 & -1 & -1 & -2 & -2 & -2 & -2 \\ 4 & -2 & -2 & -2 & -2 & 1 & 1 & 1 & 1 \\ 0 & 1 & 0 & -1 & 0 & 1 & -1 & -1 & 1 \\ 0 & -2 & 0 & 2 & 0 & 1 & -1 & -1 & 1 \\ 0 & 0 & 1 & 0 & -1 & 1 & 1 & -1 & -1 \\ 0 & 0 & -2 & 0 & 2 & 1 & 1 & -1 & -1 \\ 0 & 1 & -1 & 1 & -1 & 0 & 0 & 0 & 0 \\ 0 & 0 & 0 & 0 & 0 & 1 & 1 & 1 & -1 \end{bmatrix} \quad (6)$$

The matrix S^σ in Eq. (1) is the diagonal relaxation matrix:

$$S^\sigma = diag \left[s_\rho^\sigma, s_e^\sigma, s_\varepsilon^\sigma, s_j^\sigma, s_q^\sigma, s_j^\sigma, s_q^\sigma, s_v^\sigma, s_v^\sigma \right] \quad (7)$$

where s_ρ^σ and s_j^σ ensure the conservation of mass and momentum, respectively, and their values are equal to 1. The nonconserved moments s_e^σ, s_ε^σ, and s_q^σ are independently adjusted to improve the accuracy and stability of the simulation. In this work, the three parameters are taken as $s_e^\sigma = 0.6$, $s_\varepsilon^\sigma = 1.54$, and $s_q^\sigma = 1.2$ (Zhao et al., 2017); s_v^σ is the dimensionless relaxation time and is related to the fluid viscosity:

$$\upsilon_\sigma = c_s^2 \left(\frac{1}{s_v^\sigma} - \frac{1}{2} \right) \delta_t \quad (8)$$

where c_s denotes lattice speed velocity ($c_s^2 = 1/3$).

The force term $\overline{F}_i^\sigma$ in Eq. (1) adopts Guo's force scheme (Guo et al., 2002a):

$$\overline{F}_i^\sigma = \frac{\boldsymbol{F}^\sigma \cdot (\boldsymbol{e} - \boldsymbol{u}^{eq})}{\rho_\sigma c_s^2} f_i^{\sigma(eq)} \quad (9)$$

where $\boldsymbol{F}^\sigma$ is the total force exerted on the component σ and can be divided into three parts: fluid-fluid interaction force ($\boldsymbol{F}_f^\sigma$), fluid-solid interaction force ($\boldsymbol{F}_{ads}^\sigma$), and body force ($\boldsymbol{F}_b^\sigma$),

such as:

$$\boldsymbol{F}^\sigma = \boldsymbol{F}_f^\sigma + \boldsymbol{F}_{ads}^\sigma + \boldsymbol{F}_b^\sigma \quad (10)$$

The fluid-fluid interaction force is estimated by:

$$\boldsymbol{F}_f^\sigma(x) = -g_{\sigma\overline{\sigma}} \psi_\sigma(\boldsymbol{x}) c_s^2 \sum_{i=1}^N \omega(|\boldsymbol{e}_i|^2) \psi_{\overline{\sigma}}(\boldsymbol{x} + \boldsymbol{e}_i) \boldsymbol{e}_i \quad (11)$$

where $g_{\sigma\overline{\sigma}}$ represents the interaction parameter between the component σ and $\overline{\sigma}$. The interaction parameter between the same components ($g_{\sigma\sigma}$) is 0 because the single phase transition is not taken into account. To characterize the phase separation, the parameter between the different components is set to 0.65, which is reduced appropriately when the two-phase miscible process is considered. The parameter $\psi(x) = 1 - \exp(-\rho(x))$ is the effective mass dependent on the density of each lattice. The weights $\omega(|\boldsymbol{e}_i|^2)$ are $\omega(0) = 0$, $\omega(1) = 1/3$, and $\omega(2) = 1/12$ in the four-order isotropic discretization scheme (Chen et al., 2014).

Similar to the estimation of fluid-fluid interaction force, the fluid-solid interaction force is given by:

$$\boldsymbol{F}_{ads}^\sigma(x) = -g_{\sigma w} \psi_\sigma(\boldsymbol{x}) c_s^2 \sum_{i=1}^N \omega(|\boldsymbol{e}_i|^2) \psi(\rho_w) s(\boldsymbol{x} + \boldsymbol{e}_i) \boldsymbol{e}_i \quad (12)$$

where $g_{\sigma w}$ is the interaction parameter between the component σ and the solid, ρ_w denotes the solid density, and s is a flag function with 0 representing the fluid phase and 1 representing the solid phase. The body force is given by $\boldsymbol{F}_b^\sigma = \rho_\sigma g$ and g is the body force per unit mass.

3. Model validations

3.1 Laplace's law

The bubble test is commonly used to evaluate the interfacial tension between two phases, and can be employed to examine the accuracy of the two-phase flow model. When placing a circular droplet in the center of another immiscible liquid, the pressure difference inside and outside the droplet is proportional to the reciprocal of the droplet radius, and the slope is the interfacial tension between the two phases. The correlation is given by (Wei et al., 2022):

$$p_i - p_o = \frac{\gamma}{R} \quad (13)$$

where p_i and p_o represent the pressure inside and outside the droplet, respectively; R denotes the droplet radius; γ is the interfacial tension.

Herein, the bubble test is extended to three-phase systems. The size of the computing area is 100×100, and two concentric droplets containing the first phase and second phase with radius R_1 and R_2, respectively, are placed in the center of another immiscible third phase fluid. The initial density distribution in the calculating region is:

$$\begin{cases} \rho_1 = 1, \rho_2 = \rho_3 = 10^{-5} & (x-60)^2 + (y-60)^2 \leq R_1^2 \\ \rho_2 = 1, \rho_1 = \rho_3 = 10^{-5} & R_1^2 < (x-60)^2 + (y-60)^2 < R_2^2 \\ \rho_3 = 1, \rho_1 = \rho_2 = 10^{-5} & \text{otherwise} \end{cases} \quad (14)$$

The pressure in each lattice is estimated by (Zhao et al.,
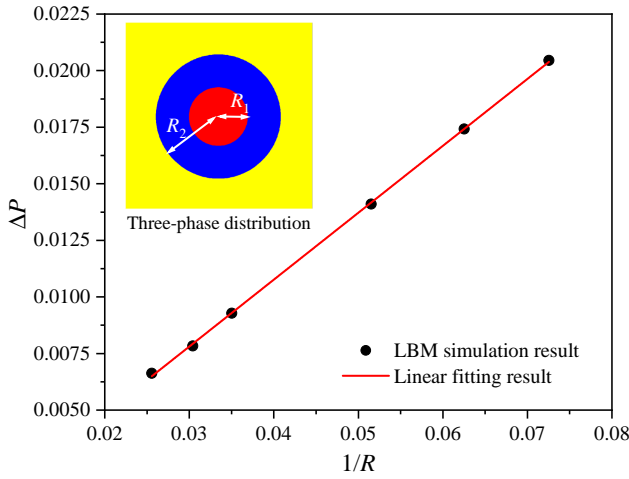
Fig. 1. Simulation result of three-phase Laplace's law. The lattice unit is used for the coordinate axes. The red, blue, and yellow regions in the inset represent the first, second, and third phase fluid, respectively.

2017):

$$p = \sum \rho_\sigma c_s^2 + \frac{c_s^2}{2} \sum g_{\sigma\overline{\sigma}} \psi_\sigma \psi_{\overline{\sigma}} \tag{15}$$

Three different cases corresponding to the R_1 values of 15, 17, and 20 are simulated. Periodic boundary condition is applied around the computational domain and there is no extra force in the entire system. The viscosity of the three phases remains the same at 1/6 (lattice unit). The maximum simulation time step is 200,000, which is sufficient for the whole system to reach a steady state. The radii of the droplets are determined from the edge of the three-phase interface, where the density is $\rho = \rho_0/2$ (ρ_0 is the initial density, i.e., 2 in this study). The pressure differences between phases 1-2 and 2-3 are estimated using the method of Chen et al. (2013). Fig. 1 indicates that there is a linear correlation between the pressure difference and the reciprocal of radius, which well agrees with Laplace's law.

3.2 Contact angle test

The static contact angle can reflect the varying wettability between different phases, which is an important parameter for multiphase flow in a porous medium. As shown in Fig. 2, the contacting droplets consisting of the first and second phases are placed on a solid plane surrounded by the third phase fluid. Subsequently, the contact angles θ_{13}, θ_{12}, and θ_{23} are obtained to characterize the wettability of the three-phase system. According to Young's equation, the correlation between contact angle and interfacial tension is given by:

$$\cos \theta_{\sigma\overline{\sigma}} = \frac{\gamma_{\overline{\sigma}w} - \gamma_{\sigma w}}{\gamma_{\sigma\overline{\sigma}}} \tag{16}$$

where $\gamma_{\overline{\sigma}w}$ and $\gamma_{\sigma w}$ represent the fluid-solid interfacial tension and $\gamma_{\sigma\overline{\sigma}}$ is the fluid-fluid interfacial tension; $\theta_{\sigma\overline{\sigma}}$ denotes the contact angle between two phases, and $\theta_{\sigma\overline{\sigma}} = \pi - \theta_{\overline{\sigma}\sigma}$.

In the MCMP Shan-Chen model, the interfacial tension is proportional to the interaction parameters given in Eqs. (11) and (12). Therefore, Eq. (16) is reformulated to more

readily predict the contact angle (Huang et al., 2007; Wei et al., 2020):

$$\cos \theta_{\sigma\overline{\sigma}} = \frac{2(g_{\overline{\sigma}w} - g_{\sigma w})}{g_{\sigma\overline{\sigma}}(\rho_{\sigma,eq} - \rho_{\overline{\sigma},dis})} \tag{17}$$

where $\rho_{\sigma,eq}$ and $\rho_{\overline{\sigma},dis}$ respectively denote the equilibrium density (i.e., 2) and the dissolved density (i.e., 10^{-5}).

The size of the calculation area is 200×100, and the top and bottom are solid walls. Initially, the first and second phases are placed on the solid wall as quarter circles (radius: 50) surrounded by the third phase. The viscosity of the three phases are identical (1/6 lattice unit). The periodic boundary condition is adopted in the four directions, and the half-way bounce-back boundary is used at the solid surface. First, six different sets of contact angles are determined. For each set of contact angles, their values are incorporated into Eq. (17) to obtain a set of equations related to fluid-solid interaction parameters. Then, the parameters are obtained by solving these equations and used to conduct the LBM simulations. These specific parameters and the simulation results are shown in Table 1 and Fig. 2, respectively. The shapes of the three-phase droplets are distinct under different parameters. The measured contact angle is consistent with the prediction of Eq. (17), which indicates that the LBM model can well characterize the different wetting conditions.

3.3 Three-phase layered flow

The layered flow between parallel plates is often used to examine the accuracy of a multiphase model. In this simulation, the size of the computational domain is 20×202, and the top and bottom are solid walls. For the initial three-phase distribution, the first phase is in the middle area of the parallel plates ($0 < |y| < a$), the third phase is located near the solid wall ($b < |y| < c$), and the second phase is between the first phase and the third phase ($a \le |y| \le b$). Periodic boundary condition is adopted in the x-direction, and half-way bounce-back boundary condition is used for the upper and lower solid walls. A body force ($F_b = 5 \times 10^{-5}$) is applied in the x-direction to mimic Poiseuille flow. The saturation of the second phase remains constant (0.2), and the regions of the first and third phases are tuned to achieve different saturations. The relative permeability of each phase under different saturations is estimated by:

$$\begin{cases} K_{r,1}(S_3) = \dfrac{\int_{|y|=0}^{a} u_1 dy}{\int_{|y|=0}^{c} u_1 dy} \\[3mm] K_{r,2}(S_3) = \dfrac{\int_{|y|=a}^{b} u_2 dy}{\int_{|y|=0}^{c} u_2 dy} \\[3mm] K_{r,3}(S_3) = \dfrac{\int_{|y|=b}^{c} u_3 dy}{\int_{|y|=0}^{c} u_3 dy} \end{cases} \tag{18}$$

where $K_{r,k}$ and S_k represent the relative permeability and saturation of the k-th phase, respectively. The denominator in the formula stands for the flow velocity of a single phase. The analytical solution for the relative permeability is related to the saturation (S_1, S_2, and S_3) and viscosity ratio (M) (Zhu et al., 2021), such as:
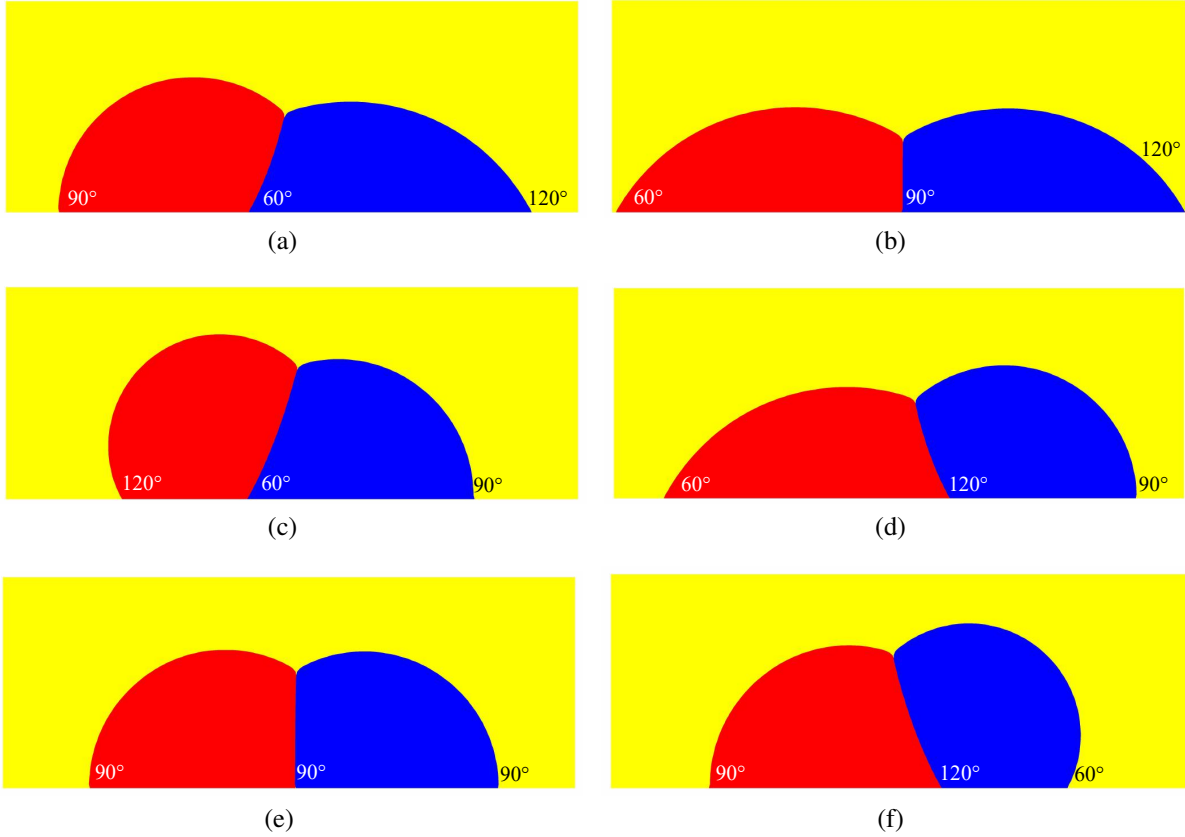
Fig. 2. LBM simulation results for different fluid-solid interaction parameters. Panels (a)-(f) correspond to the cases shown in Table 1.

Table 1. Six sets of contact angles and the corresponding fluid-solid interaction parameters.

Case	θ_{13} (°)	θ_{21} (°)	θ_{32} (°)	g_{1w}	g_{2w}	g_{3w}
a	90	60	120	0.2	-0.125	0.2
b	60	90	120	-0.2	-0.2	0.125
c	120	60	90	0.125	-0.2	-0.2
d	60	120	90	-0.125	0.2	0.2
e	90	90	90	0.2	0.2	0.2
f	90	120	60	-0.2	0.125	-0.2

$$\begin{cases} K_{r,1} = -\dfrac{3}{2}\left[\left(M_{1,2} - \dfrac{2}{3}\right)S_1^3 - (M_{1,3} \right. \\ \qquad \left. - M_{1,2})S_1(1-S_3)^2 - M_{1,3}S_1\right] \\ K_{r,2} = -\dfrac{3}{2}\left[\left(M_{2,3} - \dfrac{2}{3}\right)(1-S_3)^3 - M_{2,3}(1-S_3) \right. \\ \qquad \left. -\dfrac{1}{3}S_1^3 - (M_{2,3}-1)(1-S_3)^2 + M_{2,3}S_1\right] \\ K_{r,3} = \dfrac{1}{2}S_3^2(3-S_3) \end{cases} \quad (19)$$

where $M_{k,l} = \rho_k v_k/\rho_l v_l$ denotes the dynamic viscosity ratio between the k-th phase and l-th phase.

Three-phase viscosity ratios of 1:1:1 and 5:1:1 are simulated, and the estimated relative permeability curves are shown in Fig. 3. Notably, the relative permeability of the 1st phase is greater than 1 when the viscosity ratio M is 5:1:1. This phenomenon is normal and the reason should be attributed to the "lubrication" effect (Zhang et al. 2019; Zhu et al. 2021). Fig. 3 indicates that the simulation results are in good agreement with the analytical solution, which justifies the accuracy of the three-phase flow model.

4. Results and discussion

In this section, the three-phase Shan-Chen model is implemented to study the GDAWF process in the porous media, and the effects of water injection, viscosity ratio, pore structure, and oil-gas miscibility are explored in detail.

4.1 Comparison between direct gas displacement (DGD) and GDAWF

Two simulations are carried out to analyze the differences between DGD and GDAWF from the pore-scale perspective. The porous medium structure is adopted from the CT images of core samples in the Tarim Oilfield (Fig. 4). Two porous models in the upper and lower parts of the image are selected to carry out the three-phase flow simulation. The porosities of the two models and the original one are 0.428, 0.358, and 0.374, respectively. Their permeabilities estimated using the
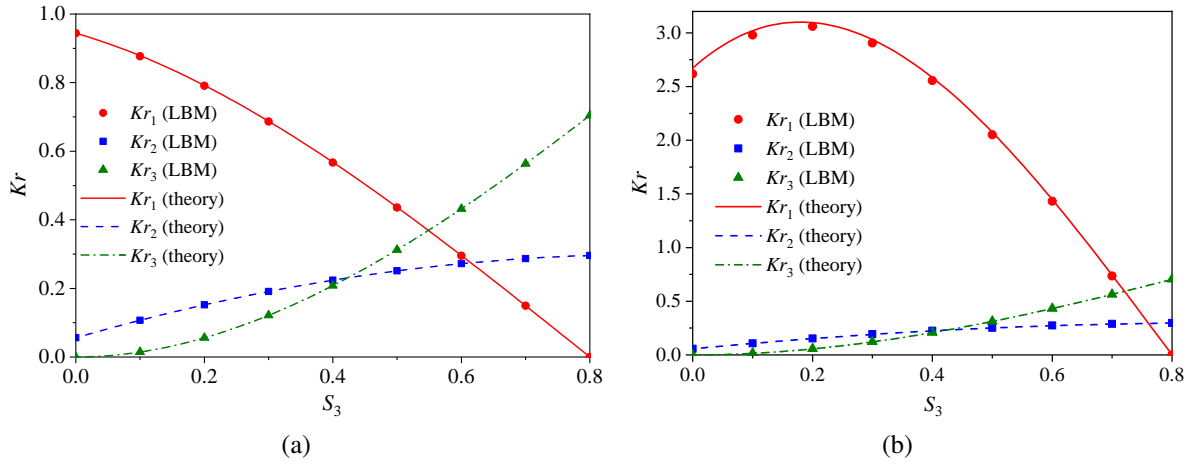
Fig. 3. Relative permeability curves for three-phase layered flow under different viscosity ratios. (a) 1:1:1 and (b) 5:1:1.
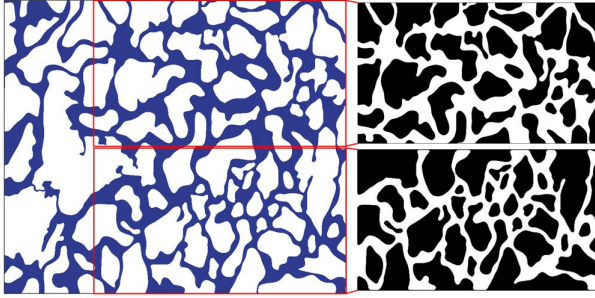
Fig. 4. The porous models used in this study. Left: the binarized image of the original CT image from the Tarim Oilfield; Right: two porous structures used for the water flooding and gas flooding simulations.

incompressible single-phase flow model (Guo et al., 2000) are 75.42×10^{-3}, 45.50×10^{-3}, and 56.28×10^{-3} μm^2, respectively. The porosities and permeabilities of the two porous models fluctuate around those of the whole porous media, which demonstrates that the porous structures are representative.

The size of the selected porous model is 680×400 lattices (corresponding to 68 $\mu m \times 40$ μm). The black and white colors represent the solid and pore region, respectively (Fig. 4). The half-way bounce-back boundary condition is utilized for the solid surface. The constant velocity boundary condition characterized using the non-equilibrium extrapolation method (Guo et al., 2002b) is used for the inlet of the porous medium (the left side). For the outlet (the right side), a fully developed boundary condition is adopted; that is, the distribution function of the lattice at the outlet boundary and the adjacent lattices are identical. To ensure the simulation stability, 30 and 170 lattices are added to the inlet and outlet of the porous model, respectively, as the buffer layers; thus, the final size of the computational area is 880×400 lattices.

During the simulation, the porous medium is first saturated with oil and then displaced with water. When the injected water reaches the outlet of the porous medium, the simulation continues for a while and then switches to gas flooding. This is because the maximum recovery of water flooding is usually not reached when the injected water has arrived at the production well, and water flooding will continue to improve the recovery.

Wettability is a multiscale property linking molecular-scale interactions with core-scale properties (Cha et al., 2022). In an actual reservoir, the wettability of the rock surface decreases in the order of water-wet, oil-wet, and gas-wet. Therefore, the fluid-solid interaction parameters of water, oil, and gas are set as -0.2, 0, and 0.3, respectively. The corresponding contact angles θ_{13}, θ_{23}, and θ_{21} estimated by Eq. (16) are 62.5°, 39.7°, and 72°, respectively. To ensure consistence with the actual conditions, the values of s_v in Eq. (7) are set as 5.5, 1, and 0.55, respectively, leading to a three-phase viscosity ratio of 100:10:1. These parameters are used in the subsequent simulations unless otherwise specified. The oil-gas interaction parameter is 0.65. To facilitate the understanding, the lattice units (lu) are converted to physical units, and the conversion factors (physical unit/lattice unit) of different physical quantities are as follows: length, 1×10^{-7} m/lu; time, $1/6 \times 10^{-8}$ s/lu; pressure difference, 1.8×10^6 Pa/lu.

During the GDAWF simulation, water is first injected for 0.5 ms and then the gas drive continues for 0.33 ms. During the DGD simulation, the gas injection time and rate remain the same as GDAWF. The simulation results of DGD shown in Fig. 5 suggest that there is an obvious gas flow path (termed gas channel) due to the reservoir heterogeneity and the large viscosity difference; thus, the gas swept area is smaller. However, owing to the smaller viscosity difference between oil and water and the reservoir hydrophilicity, water flooding shows a larger swept area during GDAWF, while the gas channel still forms after gas injection. A comparison of the two cases reveals that there are two (upper and lower) dominant channels in this porous medium. In the DGD process, the injected gas preferentially advances along the lower channel. However, in the GDAWF process, due to the existence of pre-injected water, the main flow channel of injected gas changes, which advances along the upper part of the porous model. Therefore, the pre-injected water changes the flow channel of subsequently injected gas. The simulation results at 0.25
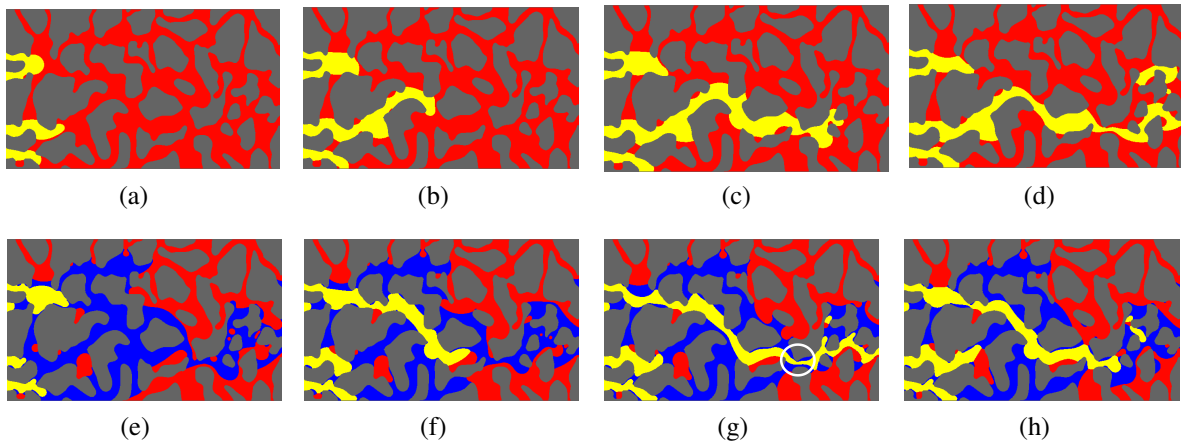
Fig. 5. Simulation results of DGD and GDAWF. (a)-(d): direct gas displacement at 0.083, 0.167, 0.25, and 0.333 ms, respectively; (e)-(f): gas displacement after water flooding at 0.583, 0.667, 0.75, and 0.833 ms, respectively (the water flooding is converted to gas flooding at 0.5 ms).
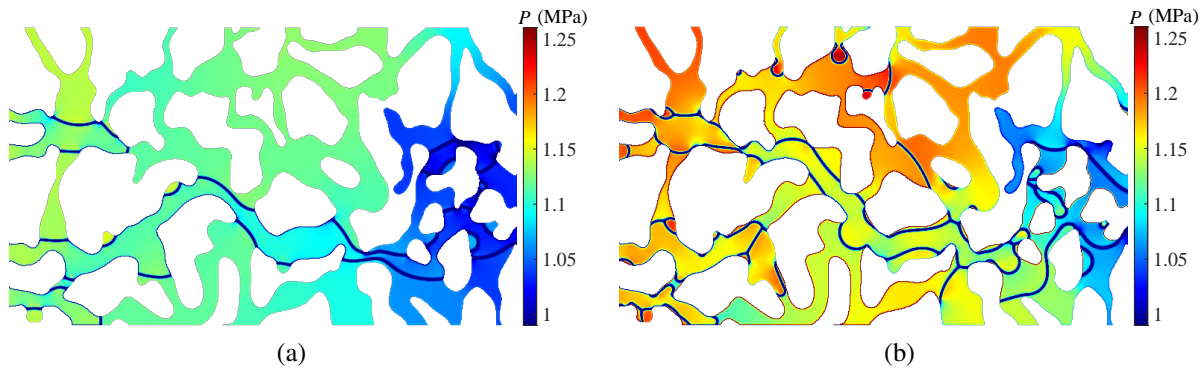
Fig. 6. Pressure distribution in the porous medium. (a) DGD 0.333 ms and (b) GDAWF 0.833 ms (the water flooding is converted to gas flooding at 0.5 ms).

ms suggest that gas channeling occurs in GDAWF but not in DGD. This should be attributed to the lower viscosity and flow resistance of water compared to oil, which makes the injected gas transport quickly through the porous medium, resulting in early gas breakthrough. Fig. 5 also indicates that there is no gas on the right side of Fig. 5(h) because gas snap-off occurs (Cha et al., 2021) in the white circle of Fig. 5(g) during the injection, and then the gas after snap-off location is expelled from the porous model in the displacement process.

Furthermore, the pressure distributions (Fig. 6) in the porous medium at the end of gas displacement are analyzed. The blue line in the figure is generated by the large pressure fluctuation at the multiphase interface, which is unphysical due to a sharp density variation and should be ignored (Chen et al., 2013). In comparison to DGD, GDAWF contains various interfaces (gas-water, oil-water, and oil-gas interfaces), which leads to a more complex pressure distribution and a larger internal pressure drop. Quantitative analysis shows that the pressure differences across the porous models are 0.086 and 0.113 MPa, respectively; therefore, GDAWF requires a higher injection pressure.

As expected, the oil recovery factor in the porous media

gradually increases with time (Fig. 7). During DGD, the recovery factor tends to be stable after gas breakthrough, which is consistent with the two-phase displacement reported by Wei et al. (2022). This is because gas forms the main flow channels inside the porous medium, it has less flow resistance and makes it difficult for the subsequent gas to spread to other areas. During GDAWF, gas displacement further enhances oil recovery by 20% over water flooding. Fig. 7(b) further reveals that the recovery factor tends to level off after gas breakthrough. However, when gas snap-off occurs, the stable gas flow channel is destroyed, and the injected gas re-enters some pores with lower flow resistance and yet again increases the recovery factor.

4.2 Effect of viscosity ratio

Large viscosity ratios can cause the viscous fingering of injected fluid. Thus, this section evaluates the effect of different oil-water-gas viscosity ratios on the GDAWF. Two different oil-water-gas viscosity ratios are simulated: 1:1:1 and 100:10:1. The values of s_v in Eq. (7) corresponding to the two cases are 1, 1, 1 and 5.5, 1, 0.55, respectively. The simulation

(a)

(b)
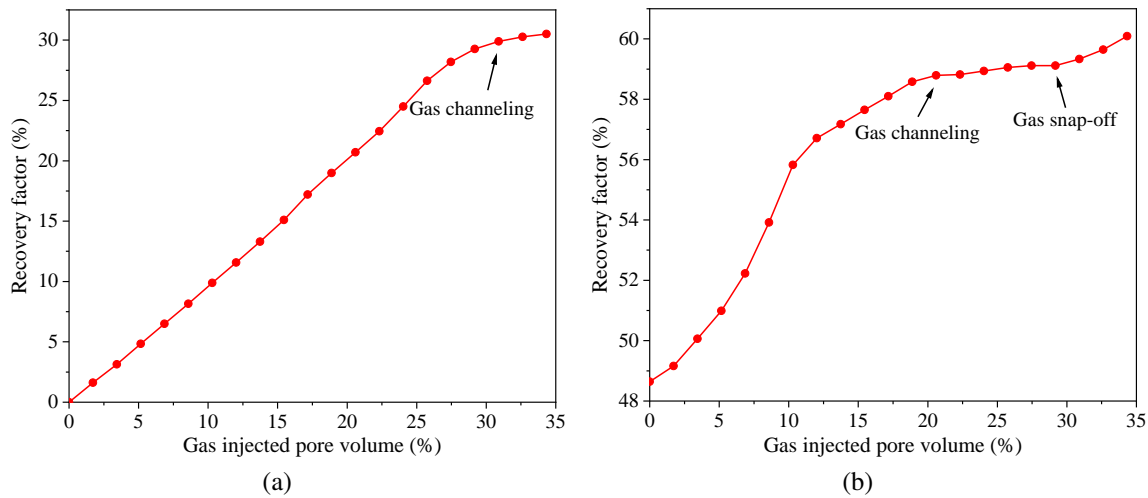
Fig. 7. Variation in the recovery factor with time during gas flooding. (a) DGD and (b) GDAWF.

(a)   (b)   (c)   (d)

(e)   (f)   (g)   (h)
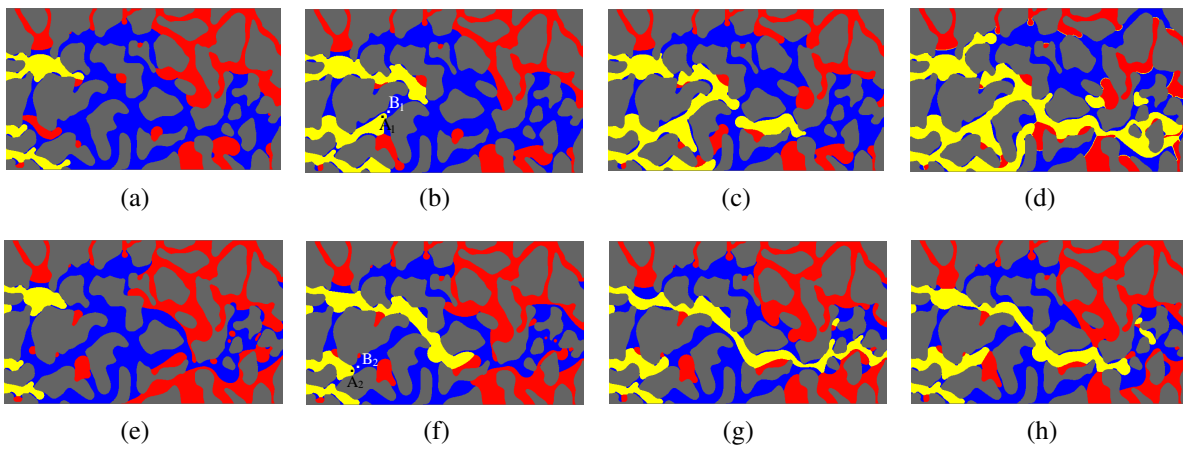
Fig. 8. Simulation result of GDAWF under different viscosity ratios. Upper panel: M = 1:1:1; lower panel: M = 100:10:1. (a)-(d) and (e)-(h) represent the different time steps: 0.583, 0.667, 0.75, and 0.833 ms, respectively (the water flooding is converted to gas flooding at 0.5 ms).
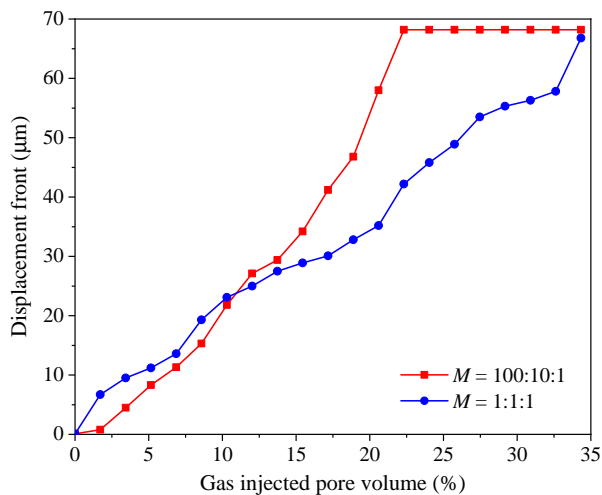
Fig. 9. Variation in the gas displacement fronts with time under different viscosity ratios.

details remain the same as reported above, and the results are shown in Fig. 8. At a lower viscosity ratio, the injected water and gas advance uniformly in the porous medium and have a greater sweeping range. When the viscosity ratio is larger, the viscosity difference between oil, water, and gas increases and viscosity fingering occurs in the porous medium, resulting in a smaller swept area. Therefore, more remaining oil is observed at the right side of the porous medium (Fig. 8).

Subsequently, the gas injection capability under different viscosity ratios is examined. The pressure difference across the gas-water interface (A_1, B_1 and A_2, B_2 in Fig. 8) under different viscosity ratios are 57.31 KPa (1:1:1) and 16.75 KPa (100:10:1), respectively, at 0.667 ms. For a higher viscosity ratio, the pressure difference across the interface is smaller, so the gas at the inlet is less likely to be displaced into the interior of the porous media, which corresponds to an increasing injection difficulty.

The positions of the gas displacement fronts under different viscosity ratios are compared in Fig. 9. At the early stage, the
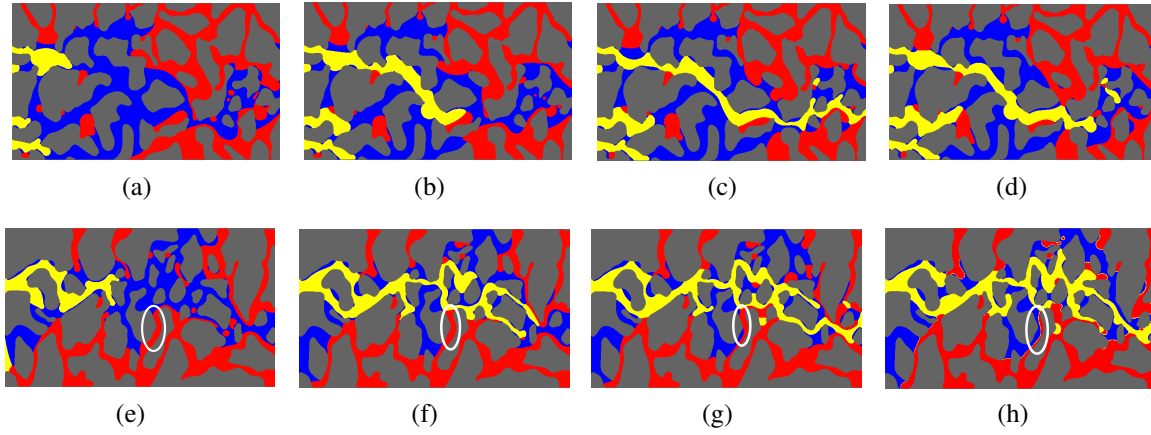
Fig. 10. Simulation result of GDAWF in the two porous models. Upper panel: porous media 1; lower panel: porous media 2. (a)-(d) and (e)-(h) represent the different time steps: 0.583, 0.667, 0.75, and 0.833 ms, respectively (the water flooding is converted to gas flooding at 0.5 ms).
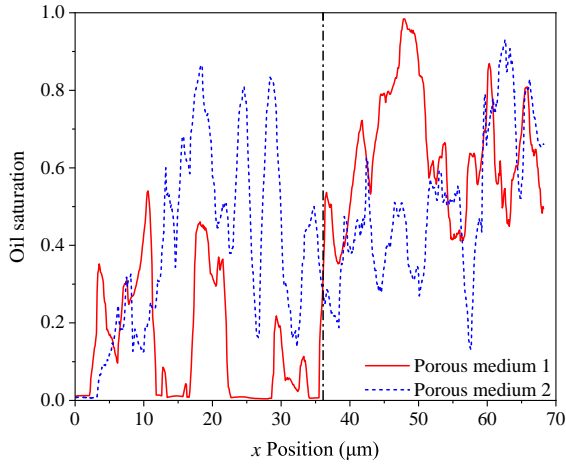
Fig. 11. Oil saturations along the flow direction in two porous models.

gas injection capability is stronger under lower viscosity conditions, and the gas front advances much faster (Fig. 9). The viscosity difference gradually appears when more gas enters the porous medium; thus, viscous fingering occurs under the condition of larger viscosity ratio, leading to the rapid advance of gas flooding front. The oil recoveries are 76.77% and 67.38% for the lower and higher viscosity ratios, respectively; therefore, the oil-water-gas viscosity ratio should be kept at a lower level to improve the effect of GDAWF.

4.3 Effect of porous structure

The pore structures in actual cores can vary greatly, which will affect the fluid flow process (Rokhforouz and Amiri, 2019). Thus, the process of GADWF in another porous model (Fig. 4) is studied. To make a direct comparison between the two models, the factor proposed by Wang et al. (2016) is used to quantitatively evaluate the heterogeneity:

$$H = \frac{1}{\phi} \sqrt{\frac{\sum (\phi_i - \phi)^2}{n-1}} \qquad (20)$$

where H represents the heterogeneity factor, n denotes the total number of divided regions in the porous medium, and ϕ_i and ϕ are the porosity of the i-th region and the total model, respectively. The estimated heterogeneity factors of the first and second porous medium are 0.2229 and 0.3306, respectively. Consequently, the second porous model is more heterogeneous.

The simulation results shown in Fig. 10 indicate that, due to the stronger heterogeneity, the injected water and gas primarily transport through the upper half, and the lower half is not swept. The oil saturations at different locations at 0.833 ms are shown in Fig. 11. Caused by the greater heterogeneity, the remaining oil saturation in the second model is higher. The increase in the remaining oil saturation in the upper half of the first porous model is attributed to viscous fingering. When observing the throat in the white circles of the second model (Fig. 10), it can be found that oil in the throat was not recovered during water flooding. However, because the rock surface is hydrophilic, water re-enters the throat under the capillary pressure during subsequent gas injection, which displaces the oil and further improves recovery (Cai et al., 2021).

4.4 Effect of oil-gas miscibility

Miscibility is an important mechanism influencing the enhancement of oil recovery in gas flooding. The miscible process basically comprises the diffusion of gas into the oil phase, which is described by Fick's second law (Mukherjee et al., 2020):

$$\frac{\partial C}{\partial t} = \nabla \cdot (D \nabla C) \qquad (21)$$

where C and D respectively denote the concentration and diffusion coefficients of the gas phase. As recommended by Wang et al. (2022), the interaction parameter g between oil and gas in Eq. (10) is set to 0.45 to take into account the miscibility. Under this condition, the gas diffusion curve is in good agreement with Fick's second law. Because the miscible
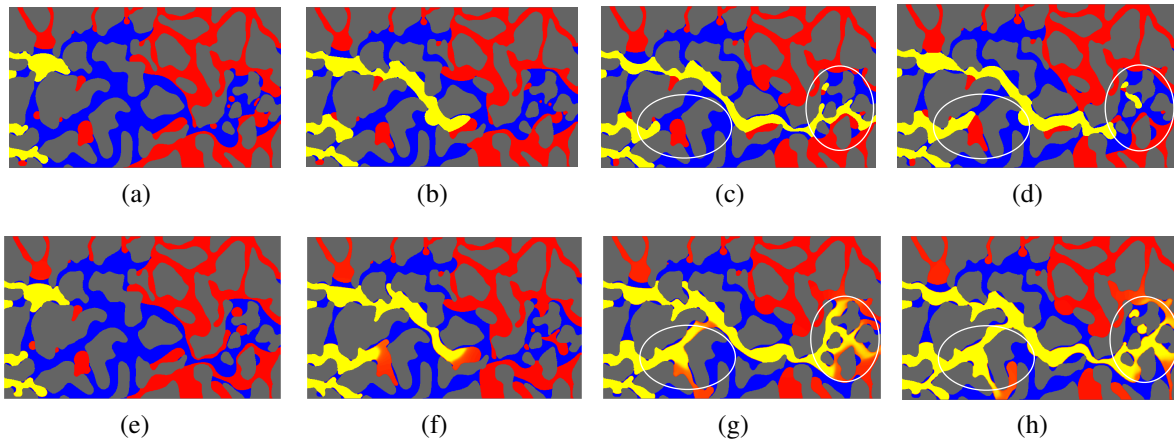
Fig. 12. Simulation result of immiscible (upper panel) and miscible (lower panel) GDAWF. (a)-(d) and (e)-(f) represent the different time steps: 0.583, 0.667, 0.75, and 0.833 ms, respectively (the water flooding is converted to gas flooding at 0.5 ms).
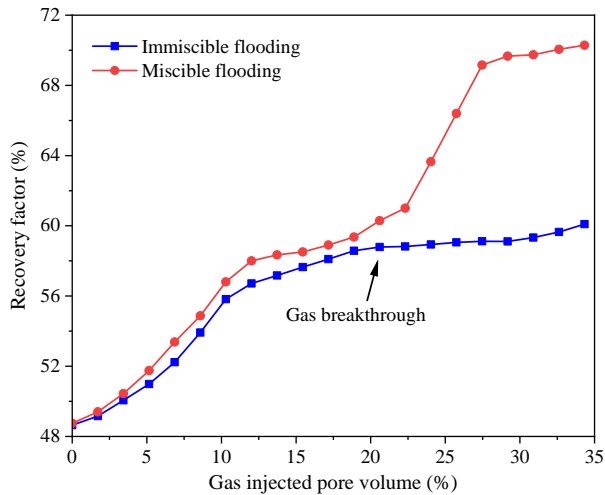
Fig. 13. Variation in the recovery factor with time during immiscible and miscible gas flooding.

process only occurs between the oil and gas phases and it cannot exist between oil-water and gas-water, their interaction parameters remain unchanged. When the gas phase meets the oil phase, the gas gradually diffuses in the oil under the concentration gradient, and the gas concentration in the oil phase continues to increases for a while. With the continued increase in the gas phase concentration, viscosity in this lattice gradually approaches that of the gas phase, which reflects the viscosity reduction effect from phase mixing. When the concentration difference on both sides of the interface is sufficiently small, the diffusion reaches the dynamic equilibrium, and the two phases become completely miscible.

The simulation results of immiscible and miscible GDAWF are shown in Fig. 12. If the injected gas does not contact oil, there is no obvious difference in the displacement process. When the gas and oil come into contact, miscibility occurs and the interface between the two phases is eliminated; thus, oil that remained at the corners during water flooding is further recovered (Fig. 13). Sohrabi et al. (2008b) reported a similar process when using microfluidic chips to study CO_2 near-

miscible displacement in porous media. By comparing the white circles in Fig. 12, it can be found that the injected gas has a larger sweep area under miscible conditions. The reason is that oil-gas miscibility increases the viscosity of the injected gas and reduces that of the oil phase, which weakens the viscosity difference between oil and gas and improves the oil transport capability. In addition, the reduced oil-gas interfacial tension after miscibility also promotes oil recovery. Therefore, to improve the production effect during gas flooding, the formation pressure should be kept higher than the oil-gas minimum miscible pressure.

5. Conclusions

In this work, we used the multi-component multi-phase Shan-Chen lattice Boltzmann model to study the three-phase flow behavior during gas displacement after water flooding, and explored the effects of water injection, viscosity ratio, pore structure, and oil-gas miscibility. The following conclusions were drawn:

1) If water flooding is taken into account, the pre-injected water will change the flow channel of injected gas, resulting in premature gas breakthrough. Meanwhile, the interfaces that are rather multiphase (oil-water, oil-gas, and water-gas interfaces) cause a more complicated pressure distribution in the porous medium and a larger pressure drop. Therefore, gas displacement after water flooding requires a higher injection pressure.

2) With the increase in the viscosity ratio, the gas fingering phenomenon is more likely to occur, which leads to a reduced gas swept area and greater remaining oil saturation. For a larger viscosity ratio, other than the preferential flow path, the injected gas tends to be trapped near the inlet and is difficult to penetrate into the porous medium, indicating an increased injection difficulty.

3) During the subsequent gas flooding, water retained in the porous medium after water injection will imbibe into the small pores under the capillary effect, which will further displace the remaining oil. When accounting for

the miscible process, the oil-gas interface disappears, eliminating the influence of capillary pressure between oil and gas phases and leading to the further recovery of the remaining oil at the corners.

Acknowledgements

Conflict of interest

The authors declare no competing interest.

References

Alemu, B., Aker, E., Soldal, M., et al. Effect of sub-core scale heterogeneities on acoustic and electrical properties of a reservoir rock: A CO_2 flooding experiment of brine saturated sandstone in a computed tomography scanner. Geophysical Prospecting, 2013, 61(1): 235-250.

Andrew, M., Bijeljic, B., Blunt, M. J. Pore-scale imaging of trapped supercritical carbon dioxide in sandstones and carbonates. International Journal of Greenhouse Gas Control, 2014, 22: 1-14.

Cai, J., Jin, T., Kou, J., et al. Lucas-Washburn equation-based modeling of capillary-driven flow in porous systems. Langmuir, 2021, 37(5): 1623-1636.

Cao, C., Liao, J., Hou, Z., et al. Utilization of CO_2 as cushion gas for depleted gas reservoir transformed gas storage reservoir. Energies, 2020, 13(3): 576.

Cha, L., Feng, Q., Wang, S., et al. Pore-scale modeling of immiscible displacement in porous media: The effects of dual wettability. SPE Journal, 2022: 1-12. (online)

Cha, L., Xie, C., Feng, Q., et al. Geometric criteria for the snap-off of a non-wetting droplet in pore-throat channels with rectangular cross-sections. Water Resources Research, 2021, 57(7): e2020WR029476.

Chen, L., Kang, Q., Mu, Y., et al. A critical review of the pseudopotential multiphase lattice Boltzmann model: Methods and applications. International Journal of Heat and Mass Transfer, 2014, 76: 210-236.

Chen, L., Kang, Q., Robinson, B. A., et al. Pore-scale modeling of multiphase reactive transport with phase transitions and dissolution-precipitation processes in closed systems. Physical Review E, 2013, 87(4): 043306.

Chen, L., Zhang, L., Kang, Q., et al. Nanoscale simulation of shale transport properties using the lattice Boltzmann method: permeability and diffusivity. Scientific Reports, 2015, 5(1): 8089.

Davarpanah, A., Mazarei, M., Mirshekari, B. A simulation study to enhance the gas production rate by nitrogen replacement in the underground gas storage performance.

Energy Reports, 2019, 5: 431-435.

Diao, Z., Li, S., Liu, W., et al. Numerical study of the effect of tortuosity and mixed wettability on spontaneous imbibition in heterogeneous porous media. Capillarity, 2021, 4(3): 50-62.

Feng, Q., Cha, L., Dai, C., et al. Effect of particle size and concentration on the migration behavior in porous media by coupling computational fluid dynamics and discrete element method. Powder Technology, 2020, 360: 704-714.

Golparvar, A., Zhou, Y., Wu, K., et al. A comprehensive review of pore scale modeling methodologies for multiphase flow in porous media. Advances in Geo-Energy Research, 2018, 2(4): 418-440.

Guo, Z., Shi, B., Wang, N. Lattice BGK model for incompressible Navier-Stokes equation. Journal of Computational Physics, 2000, 165(1): 288-306.

Guo, Z., Zheng, C., Shi, B. Discrete lattice effects on the forcing term in the lattice Boltzmann method. Physical Review E, 2002a, 65(4): 046308.

Guo Z., Zheng, C., Shi, B. Non-equilibrium extrapolation method for velocity and pressure boundary conditions in the lattice Boltzmann method. Chinese Physics, 2002b, 11(4): 366.

Huang, H., Thorne, D. T., Schaap, M. G., et al. Proposed approximation for contact angles in Shan-and-Chen-type multicomponent multiphase lattice Boltzmann models. Physical Review E, 2007, 76(6): 066701.

Hustad, O. S., Holt, T. Gravity stable displacement of oil by hydrocarbon gas after waterflooding. Paper SPE 24116 Presented at the SPE/DOE Enhanced Oil Recovery Symposium, Tulsa, Oklahoma, 22-24 April, 1992.

Ji, S., Tian, C., Shi, C., et al. New understanding on water-oil displacement efficiency in a high water-cut stage. Petroleum Exploration and Development, 2012, 39(3): 362-370.

Kong, D., Gao, Y., Sarma, H., et al. Experimental investigation of immiscible water-alternating-gas injection in ultra-high water-cut stage reservoir. Advances in Geo-Energy Research, 2021, 5(2): 139-152.

Li, S., Liu, H., Zhang, J., et al. Modeling of three-phase displacement in three-dimensional irregular geometries using a lattice Boltzmann method. Physics of Fluids, 2021, 33(12): 122108.

Li, Q., Luo, K., Li, X. Lattice Boltzmann modeling of multiphase flows at large density ratio with an improved pseudopotential model. Physical Review E, 2013, 87(5): 053301.

Liu, Y., Chen, M., Sun, S., et al. Effects of grain shape and packing pattern on spontaneous imbibition under different boundary conditions: Pore-scale simulation. Journal of Hydrology, 2022a, 607: 127484.

Liu, H., Kang, Q., Leonardi, C. R., et al. Multiphase lattice Boltzmann simulations for porous media applications. Computational Geosciences, 2016, 20(4): 777-805.

Liu, S., Ren, B., Li, H. Y., et al. CO_2 storage with enhanced gas recovery (CSEGR): A review of experimental and numerical studies. Petroleum Science, 2022b, 19(2): 594-

607.

Liu, J., Wang, S., Javadpour, F., et al. Hydrogen diffusion in clay slit: Implications for the geological storage. Energy & Fuels, 2022c, 36(14): 7651-7660.

Mazarei, M., Davarpanah, A., Ebadati, A., et al. The feasibility analysis of underground gas storage during an integration of improved condensate recovery processes. Journal of Petroleum Exploration and Production Technology, 2019, 9(1): 397-408.

Mukherjee, S., Dang, S. T., Rai, C., et al. Novel techniques to measure oil-gas diffusion at high pressure & high temperature conditions: Application for huff-n-puff EOR in shale. Paper URTEC 20202203 Presented at the SPE/AAPG/SEG Unconventional Resources Technology Conference, Virtual, 20-22 July, 2020.

Preston, C., Monea, M., Jazrawi, W., et al. IEA GHG Weyburn CO_2 monitoring and storage project. Fuel Processing Technology, 2005, 86(14): 1547-1568.

Qu, M., Hou, J., Wen, Y., et al. Nitrogen gas channeling characteristics in fracture-vuggy carbonate reservoirs. Journal of Petroleum Science and Engineering, 2020, 186: 106723.

Ren, B., Male, F., Duncan, I. J. Economic analysis of CCUS: Accelerated development for CO_2 EOR and storage in residual oil zones under the context of 45Q tax credit. Applied Energy, 2022, 321: 119393.

Ren, B., Ren, S., Zhang, L., et al. Monitoring on CO_2 migration in a tight oil reservoir during CCS-EOR in Jilin oilfield China. Energy, 2016, 98: 108-121.

Rokhforouz, M. R., Akhlaghi Amiri, H. A. Effects of grain size and shape distribution on pore-scale numerical simulation of two-phase flow in a heterogeneous porous medium. Advances in Water Resources, 2019, 124: 84-95.

Shen, H., Yang, Z., Li, X., et al. CO_2-responsive agent for restraining gas channeling during CO_2 flooding in low permeability reservoirs. Fuel, 2021, 292: 120306.

Sohrabi, M., Danesh, A., Jamiolahmady, M. Visualisation of residual oil recovery by near-miscible gas and SWAG injection using high-pressure micromodels. Transport in Porous Media, 2008a, 74(2): 239-257.

Sohrabi, M., Danesh, A., Tehrani, D. H., et al. Microscopic mechanisms of oil recovery by near-miscible gas injection. Transport in Porous Media, 2008b, 72(3): 351-367.

Tang, M., Zhan, H., Lu, S., et al. Pore-scale CO_2 displacement simulation based on the three fluid phase lattice Boltzmann method. Energy & Fuels, 2019, 33(10): 10039-10055.

Tovar, F. D., Eide, Ø., Graue, A., et al. Experimental investigation of enhanced recovery in unconventional liquid reservoirs using CO_2: A look ahead to the future of unconventional EOR. Paper SPE 169022 Presented at the SPE Unconventional Resources Conference, The Woodlands, Texas, USA, 1-3 April, 2014.

Wang, Z., Jin, X., Sun, L., et al. Pore-scale geometry effects on gas permeability in shale. Journal of Natural Gas Science and Engineering, 2016, 34: 948-957.

Wang, H., Su, Y., Wang, W., et al. CO_2-oil diffusion, adsorption and miscible flow in nanoporous media from pore-scale perspectives. Chemical Engineering Journal, 2022, 450: 137957.

Wang, H., Yuan, X., Liang, H., et al. A brief review of the phase-field-based lattice Boltzmann method for multiphase flows. Capillarity, 2019, 2(3): 33-52.

Wei, B., Hou, J., Sukop, M. C., et al. Enhancing oil recovery using an immiscible slug: Lattice Boltzmann simulation by three-phase pseudopotential model. Physics of Fluids, 2020, 32(9): 092105.

Wei, H., Zhu, X., Liu, X., et al. Pore-scale study of drainage processes in porous media with various structural heterogeneity. International Communications in Heat and Mass Transfer, 2022, 132: 105914.

Yu, Y., Liang, D., Liu, H. Lattice Boltzmann simulation of immiscible three-phase flows with contact-line dynamics. Physical Review E, 2019, 99(1): 013308.

Zeidan, D., Bähr, P., Farber, P., et al. Numerical investigation of a mixture two-phase flow model in two-dimensional space. Computers & Fluids, 2019, 181: 90-106.

Zhang, J. Lattice Boltzmann method for microfluidics: Models and applications. Microfluid Nanofluid, 2011, 10(1): 1-28.

Zhang, C., Chen, L., Ji, W., et al. Lattice Boltzmann mesoscopic modeling of flow boiling heat transfer processes in a microchannel. Applied Thermal Engineering, 2021, 197: 117369.

Zhang, D., Li, S., Jiao, S., et al. Relative permeability of three immiscible fluids in random porous media determined by the lattice Boltzmann method. International Journal of Heat and Mass Transfer, 2019, 134: 311-320.

Zhao, H., Ning, Z., Kang, Q., et al. Relative permeability of two immiscible fluids flowing through porous media determined by lattice Boltzmann method. International Communications in Heat and Mass Transfer, 2017, 85: 53-61.

Zhao, F., Wang, P., Huang, S., et al. Performance and applicable limits of multi-stage gas channeling control system for CO_2 flooding in ultra-low permeability reservoirs. Journal of Petroleum Science and Engineering, 2020, 192: 107336.

Zhu, X., Chen, L., Wang, S., et al. Pore-scale study of three-phase displacement in porous media. Physics of Fluids, 2022, 34(4): 043320.

Zhu, X., Wang, S., Feng, Q., et al. Pore-scale numerical prediction of three-phase relative permeability in porous media using the lattice Boltzmann method. International Communications in Heat and Mass Transfer, 2021, 126: 105403.